The *in situ* generated emerging phase inside dual phase oxygen transport membranes

Ke Ran [a,b,*], Fanlin Zeng [c], Liudmila Fischer [c,d], Stefan Baumann [c], Wilhelm A. Meulenberg [c,d], Kerstin Neuhaus [e], Joachim Mayer [a,b]

[a] *Central Facility for Electron Microscopy GFE, RWTH Aachen University, Aachen 52074, Germany*
[b] *Ernst Ruska-Centre for Microscopy and Spectroscopy with Electrons ER-C, Forschungszentrum Jülich GmbH, Jülich 52425, Germany*
[c] *Institute of Energy and Climate Research IEK-1, Forschungszentrum Jülich GmbH, Jülich 52425, Germany*
[d] *Faculty of Science and Technology, Inorganic Membranes, University of Twente, Enschede 7500 AE, the Netherlands*
[e] *Institute of Energy and Climate Research IEK-12, Helmholtz-Institute Münster, Forschungszentrum Jülich GmbH, Münster 48149, Germany*

ARTICLE INFO

ABSTRACT

The *in situ* generated emerging phase inside the dual-phase oxygen transport membranes (DP-OTMs) plays a crucial role in boosting the overall performance of DP-OTMs. However, its detailed structure and properties are still not fully understood. Utilizing advanced transmission electron microscopy (TEM) techniques, the emerging phase $Gd_xCe_{1-x}Fe_yCo_{1-y}O_{3-\delta}$ (GCFCO) inside the $Ce_xGd_{1-x}O_{2-\delta}$-$FeCo_2O_4$ (CGO-FC2O) OTMs was successfully characterized at the atomic scale. The newly formed GCFCO is primarily surrounded by the CGO, and contributes to a significant reduction of non-solute segregation at the CGO grain boundaries. Electronic characteristics of the GCFCO shows a sensitive dependence on its chemical composition, including the valence state of Ce and Fe as well as the oxygen vacancies. Additional CGO-GCFCO interfaces were introduced, where almost intact crystal structures were observed with slight Gd and Co segregation $\sim$1 nm at the edges. Approaching the interface, on the CGO side, only a minimum drop of the Ce valence was determined. On the GCFCO side, mixed Ce^{3+} and Ce^{4+} are partially occupying the Gd sites, while Fe and Co valence stay constant until the edge. Our study provides novel insight into the phase information within CGO-FC2O composites, which paves the path towards superior performance of various DP-OTMs.

© 2022 Acta Materialia Inc. Published by Elsevier Ltd. All rights reserved.

1. Introduction

With the ever-increasing demands for O_2, the search for cost-effective oxygen permeable membranes is urgent [1,2]. As an attractive alternative to the single phase oxygen transport membranes [3,4], dual phase oxygen transport membranes (DP-OTMs) with interpenetrating networks of electron conducting and ion conducting components are combining a reasonable oxygen flux with high mechanical and chemical stability under reaction conditions [1,5–8]. Continous efforts are still being made to further improve their performance, via basic adaptation of the composition, precise control of the phase interaction, as well as full optimization of the interfaces between the individual constituents.

Among the DP-OTMs, an oxygen ion-conducting Gd doped CeO_2 mixed with an electron-conducting $FeCo_2O_4$ spinel phase, CGO-FC2O, is receiving increasing attention [5,9,10]. Inside many CGO-FC2O composites, an emerging phase with the $GdFeO_3$ perovskite structure was often identified above a processing temperature of 1050 °C [11], along with newly introduced interfaces. Similar perovskite phases were also employed as a primary phase in some DP-OTMs [12–14], providing a mixed ionic and electronic conductivity. Inside CGO-FC2O, the emerging perovskite phase is expected to complex the conducting paths, and further affect the transport of charge carriers through the membrane. Thus, a proper control of the emerging phase could facilitate promotions of ionic and electronic transport inside CGO-FC2O. In this respect, precise understanding of the structure and chemistry of the emerging phase, as well as its behaviors at different interfaces, where a variety of reactions and elemental diffusions could occur, would be however the key for success.

For many oxides, advanced high-resolution transmission electron microscopy (TEM) has been utilized to reveal the atomic structure of internal defects [15,16], the presence of non-stoichiometry at grain boundaries (GBs) [17–20] and dislocation cores [21,22]. Applying it to CGO-FC2O, the emerging phase could be probed with atomic resolution. However, such studies have

---

* Corresponding author at: Central Facility for Electron Microscopy GFE, RWTH Aachen University, Aachen 52074, Germany.
 E-mail address: ran@gfe.rwth-aachen.de (K. Ran).

been rarely reported. In this work, combining scanning transmission electron microscopy (STEM), energy-dispersive X-ray spectroscopy (EDXS) and electron energy loss spectroscopy (EELS), we will focus on the emerging phase inside CGO-FC2O. Apart from its formation and structure, emerging phases with different compositions will be compared, casting light on the fine tuning of phase interactions. The newly introduced interfaces especially between the emerging phase and CGO will be investigated in detail, as they replace the original CGO GBs and are thus directly related to the ionic conductivity of the membranes. Moreover, effects of the emerging phases on the primary CGO phase will be discussed. With a comprehensive characterization of the emerging phase inside CGO-FC2O down to sub-nm scale, indispensable insights for membrane optimization will be provided from various aspects.

2. Materials and methods

Dense pellets with three different nominal compositions, i.e. 85 wt.% $Ce_{0.8}Gd_{0.2}O_{2-\delta}$:15 wt.% Fe_2CoO_4 (85CGO20-F2CO), 85 wt.% $Ce_{0.9}Gd_{0.1}O_{2-\delta}$:15 wt.% $FeCo_2O_4$ (85CGO10-FC2O), and 60 wt.% $Ce_{0.8}Gd_{0.2}O_{2-\delta}$:40 wt.% $FeCo_2O_4$ (60CGO20-F2CO)were prepared by solid state reactive sintering (SSRS) method [11,23,24]. The nominal compositions refers to the initial ratio of Gd-doped ceria to iron cobalt oxide in the powder precursors without considering any phase interactions. To prepare the powder precursors, respective amounts of commercially available powders of CGO20 (Treibacher Industrie AG, Austria) or CGO10 (grade UHSA, Solvay, Belgium) as well as Fe_2O_3 and Co_3O_4 (Sigma-Aldrich, Germany) were homogenized by ball milling in ethanol. Details of the ball milling procedures can be found in Ref. [11]. After drying, the powder mixtures were pressed into pellets and sintered at 1200 °C for 10 h. During cooling, a slow rate of 0.5 °C/min was used between 900 and 800 °C in order to re-oxidize the rock salt phase to the desired spinel phase [5], while for the other temperature ranges, a faster cooling rate of 3 °C/min was used. In addition, to obtain a Co-free $GdFeO_3$ type perovskite phase, a compound with a nominal formula of $Ce_{0.85}Fe_{0.05}Gd_{0.1}O_{2-\delta}$ was also synthesized by a sol-gel method as reported in our previous work [25].

TEM specimens were cut from the polished cross sections of the sintered pellets by focused ion beam (FIB) milling using an FEI Strata400 system with Ga ion beam. Further thinning and cleaning were performed with an Ar ion beam in a Fischione Nanomill 1040 at 900 eV and 500 eV beam energy, respectively.

TEM, energy-filtered TEM (EFTEM) and electron diffraction were performed by FEI Tecnai F20 at 200 kV. High resolution high-angle annular dark-field (HAADF) image, EDXS chemical mapping and EELS spectrum imaging (EELS SI) with atomic resolution were conducted with an FEI Titan G2 80-200 ChemiSTEM microscope equipped with an XFEG, a probe Cs corrector, a super-X EDXS system, and a Gatan Enfinium ER (model 977) spectrometer with DUAL EELS acquisition capability [26]. The convergence semi-angle for STEM imaging and EDXS chemical mapping was approximately 22 mrad, while the collection semi-angles were 80–220 mrad for HAADF imaging and around 47 mrad for EELS SI. EDXS maps were collected typically for around 10 min, and background subtraction was performed. EELS SIs were recorded with 0.5 eV per channel energy dispersion and 0.1 s dwell time for each pixel. Energy drift was corrected by aligning the zero-loss peak (ZLP) that was acquired simultaneously with core edges via dual EELS mode. Multivariate statistical analysis (MSA) was performed to reduce the noise of the EEL spectra with weighted principle-component analysis (PCA). To improve the image quality, the HAADF images were first averaged from a series of frames with a relatively short exposure time by an iterative rigid alignment algorithm, and then smoothed by a non-linear filtering algorithm [17]. Structural models were visualized with VESTA [27].

3. Results

3.1. Formation and structure of the emerging phase

Fig. 1a and b compare the grain and phase distribution of two composites, i.e. nominal 85CGO10-FC2O and 85CGO20-FC2O. Grain sizes of ∼ hundreds of nms can be determined for both composites from the left TEM images. The corresponding EFTEM images at the middle in Fig. 1a and b separate the CGO (red) and FC2O (green), revealing a homogeneous mixture of the two primary phases in both composites. Clear differences are however noticed in the Gd maps. In Fig. 1a, the uniformly distributed Gd is consistent with Ce (as compared with the Ce+Co map), corresponding to the doped Gd in ceria and suggesting a dual phase composite free of any emerging phase. In contrast to the evenly distributed intensity, the Gd in Fig. 1b is significantly concentrated at several grains, as marked by the arrows. Interestingly, these Gd-rich grains coincide with the dark regions in the Ce+Co map, indicating that these grains belongs to neither of the primary phases (CGO or FC2O) but to an emerging phase. Moreover, it also shows that these emerging phase grains are mainly surrounded by CGO20 grains.

In order to identify the emerging phase as marked by the arrows in Fig. 1b, comprehensive TEM techniques were utilized. Fig. 1c shows a HAADF image of the emerging phase with the corresponding diffraction pattern at the lower left. Together with diffraction patterns recorded along other zone axes (Supporting information, Fig. S1), a crystal structure fitting best with our experimental results is the $GdFeO_3$ (GFO) [28]. As shown in Fig. 1d, the orthorhombic perovskites GFO is derived from the ideal cubic structure *Pm3m* via titling and distortion of the BO_6 octahedra. It has a general stoichiometry ABO_3, and belongs to the space group *Pbnm*. Thus, the results in Fig. 1c can be indexed as along the [110] direction of GFO, which also shows a good agreement with the correspondingly oriented GFO model in Fig. 1e.

Chemical structure of the emerging phase is further probed by EDX elemental mapping with atomic resolution. Keeping the sample along [110] direction, Fig. 1f shows the simultaneously recorded HAADF image and elemental maps. The atomic columns of both Gd and Fe are clearly resolved, consistent with the GFO model. Local maxima are noticed in the Ce and Co map as well, which basically coincide with the Gd and Fe map respectively. Moreover, line profiles along the arrow as indicated in the HAADF image is plotted at the bottom of Fig. 1f. Peaks of Gd/Fe and Ce/Co (lower in intensity and randomly distributed) are located simultaneously with the brighter/darker atomic columns in the HAADF image. Thus, the emerging phase observed in the 85CGO20-FC2O system can be determined as GCFCO, adopting the GFO structure with the Gd and Fe sites partially occupied by Ce and Co respectively.

3.2. Composition and valence states of the emerging phase

The emerging phase GCFCO in Fig. 1f, and another one without Co i.e. GCFO from a compound of $Ce_{0.85}Fe_{0.05}Gd_{0.1}O_{2-\delta}$ (Supporting information, Fig. S2) [25], are compared here to reveal the compositional effect on the electronic features. Similar as in Fig. 1f, the GCFO grain was oriented along the [110] direction for EDX chemical mapping (Supporting information, Fig. S3), and all the spectra were collected from grain interiors to avoid any interface effect. In Fig. 2a and b, the integrated EDX spectra from both phases are plotted, together with fitted peaks using Gaussian function. Clearly, the Co $K\alpha$ and $L\alpha$ (∼0.775 keV) peak are disappearing in Fig. 2b, and the relative heights between Gd $L\alpha$ and Fe $K\alpha$ are reverse in Fig. 2a and b. The composition of GCFCO in Fig. 1f was determined as $Gd_{0.58}Ce_{0.42}Fe_{0.69}Co_{0.31}O_{3-\delta}$ based on calculations using XRD data [24]. Taking it as a reference, the *k* factors can be cali-
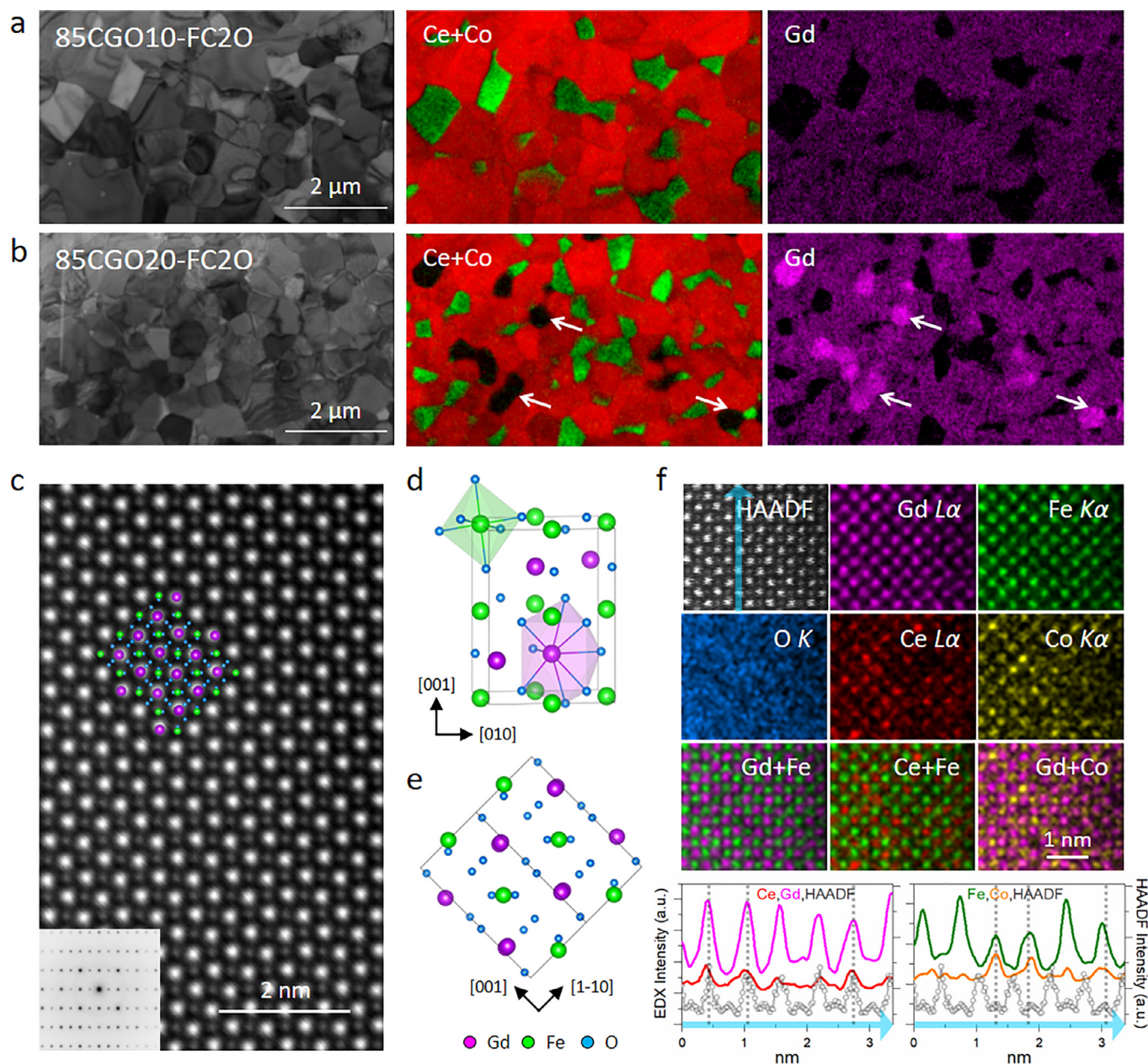
Fig. 1. Determination of the emerging phase. (a,b) TEM and the corresponding EFTEM images from 85CGO10-FC2O and 85CGO20-FC2O (red: Ce and thus representing CGO, green: Co and thus representing FC2O, magenta: Gd). Arrows in (b) are marking the same locations in both the Ce+Co and the Gd map. (c) HAADF image and the corresponding diffraction pattern from the emerging phase, later indexed as along the [110] zone axis of GFO. (d) Structural model of the GFO, highlighting two polyhedra centered around Gd and Fe respectively. (e) The GFO model viewed along [110] direction. It is also overlaid on the HAADF image in (c) for comparison. (f) EDX chemical mapping results along [110] direction: HAADF image, elemental maps from Gd $L\alpha$ line, Ce $L\alpha$ line, Fe $K\alpha$ line, Co $K\alpha$ line, O K line, and composite maps of Gd, Fe, Ce and Co. Intensity profiles along the arrow in the HAADF image are plotted at the bottom, and a few peaks of Ce and Co are marked by the dotted lines.

brated and used to estimate the atomic composition of the GCFO [17]. As shown in Table 1, 29% of the Gd sites are occupied by Ce insidie GCFO, obviously lower than the 42% inside GCFCO. Without any Co, the Fe sites are fully occupied by Fe. It's worth to note that the O content in GCFO is much higher ($\sim$22% more) than that in GCFCO. As a result, considerably more oxygen vacancies would be expected inside the GCFCO as compared with GCFO.

Furthermore, EELS SI was performed for both phases from grain interiors (Supporting information, Fig. S4). The integrated EEL spectra from GCFCO and GCFO are first aligned in respect to the Gd $M_{4,5}$, and the major edges are plotted in Fig. 2c. The O K edges are quite similar. Slight differences include a thinner peak A and a more significant peak B in GCFO, as marked by the dotted lines.

The Fe $L_{2,3}$ edges from GCFO shift to the right comparing with those from the GCFCO. Relative shift of the Ce $M_{4,5}$ edges between the GCFCO and GCFO are also noticed. Besides, the M_4 edge is significantly lower than the M_5 edge in GCFO. Quantitatively, based on the Ce M_5/M_4 intensity ratio in second derivative spectra [29,30], the Ce valence state are estimated as $\sim$3.5 and $\sim$3.2 for GCFCO and GCFO respectively in Table 1. The valence-specific multiplet structures of the Fe $L_{2,3}$ edges also enable an estimation of the Fe valence states [31]. As listed in Table 1, $\sim$82% of the Fe at the Fe sites are 3+ in GCFCO, while the ratio increases to $\sim$89% in GCFO. For Co, the white line intensity ratios are calculated as $\sim$4.5 [32,33], suggesting a partial occupation of the Fe sites by pure Co^{2+}.
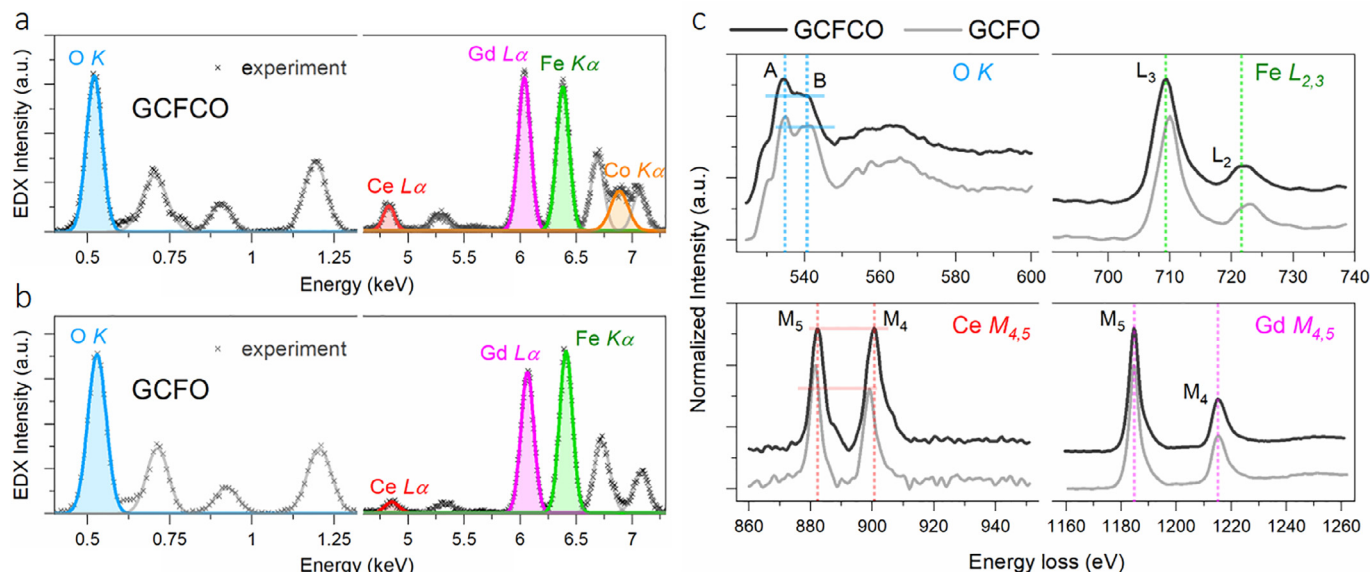
Fig. 2. The comparison between GCFCO and GCFO. (a) Spectrum from the EDX mapping in Fig. 1f, after background subtraction. All peaks are fitted with Gaussian function (the solid lines). (b) The EDX spectrum collected from a GCFO grain by tilting it along the [110] zone axis (Supporting information, Fig. S3). The filled O K, Ce $L\alpha$, Gd $L\alpha$ and Fe $K\alpha$ are further integrated for quantification. (c) The EEL spectra from GCFCO and GCFO (Supporting information, Fig. S4), comparing the O K, Fe $L_{2,3}$, Ce $M_{4,5}$ and Gd $M_{4,5}$ edges.

Table 1
The determined chemical compositions and valence states based on the EDX and EELS SI results in Fig. 2.

EDX						EELS				
	Gd	Ce	Fe	Co	O	Ce M_5/M_4 ratio	Ce valence	Fe L_3/L_2 ratio	Fe^{3+}/ΣFe (%)	Co L_3/L_2 ratio
GCFCO	0.58	0.42	0.69	0.31	x	1.09$\pm$0.00	3.48$\pm$0.01	7.76$\pm$0.10	82.22$\pm$0.89	4.49$\pm$ 0.07
GCFO	0.71$\pm$0.02	0.29$\pm$0.02	1	—	(1.22$\pm$0.04)•x	1.19$\pm$0.00	3.19$\pm$0.00	8.52$\pm$0.03	88.95$\pm$0.29	—

3.3. The CGO20-GCFCO interface

As shown in Fig. 1b, the emerging GCFCO is primarily surrounded by CGO20. Thus, mainly CGO20-GCFCO interfaces will be introduced to the system, which replace the original CGO GBs. Since the overall performance of a DP-OTM is largely dependent on the CGO GBs [10,34,35], these newly formed CGO20-GCFCO interfaces would be then especially important, as they will participate in determining whether the GCFCO phase serves as a blocker or promoter for oxygen ion transport.

In Fig. 3a, a CGO20-GCFCO interface is viewed quasi edge-on, with the GCFCO grain on the left side along its [110] direction. A clean interface is observed, and the crystal structure of GCFCO keeps almost intact until the edge as outlined by its (001) and (1-10) planes. In addition to the crystal structure, chemical disorder around the interface is probed by EELS as well. Fig. 3b shows the EELS SI results: the simultaneously recorded annular dark-field (ADF) image, together with the extracted elemental maps. The atomic columns of Gd, Fe and O on the GCFCO side can be well resolved. Around the interface, a slight Co enrichment and a clear drop of O are noticed. As indicated at the top of the ADF image, the whole mapping area is divided into ten sub-regions, R1-10, and Fig. 3c further plots the vertically averaged distribution of each element. Both Ce and Fe vary smoothly across the interface, while O drops abruptly with a minimum value at R7. The Co is locally enriched around R5-6, and a quite broad hillock mainly within R7-8 is noticed along the Gd profile, as highlighted by the filled areas. Thus, the CGO20-GCFCO interface should be between R6 and R7, with ~1 nm thick Co and Gd segregated to the edge of the GCFCO and CGO20 [19], respectively.

Moreover, Fig. 3d compares the EEL spectra integrated from each sub-region. For the O K edges, spectra from R1-6 (GCFCO side) are clearly different from those from R7-10 (CGO20 side), where several primary peaks are labeled as A-C and A'-C' respectively. Among R1-6, positions of peak A-C stay consistently, while peak A and C are fading away in R5-6. On the CGO20 side, both peak A' and C' keep rising from R7-10. All the Fe $L_{2,3}$ and Co $L_{2,3}$ edges in Fig. 3d are quite similar, and due to the extremely low solubility of Fe and Co inside ceria [36,37], any signals from R7-10 are rather ignorable and thus not plotted here. For Ce $M_{4,5}$, no significant shift of the $M_{4,5}$ edges can be observed, but the height difference between M_5 and M_4 edges are getting larger from R1 to R10, as marked by the dashed lines.

The Ce valence states are then estimated for each sub-region, in Fig. 3e top. On the GCFCO side and away from the interface (R1-3), mixed Ce^{3+} and Ce^{4+} are partially occupy the Gd sites, with an averaged valence of ~3.65. Starting from R4, the Ce valence increases steadily from ~3.69 to ~3.94 at R8, and finally stays ~4 on the CGO20 side (R9-10). A Fe^{3+}/ΣFe value of ~85.03% is constantly determined for R1-5. At R6, a slight drop to ~83.72% is noticed, but could be resulting from the poor signal to noise ratio at the interface. As shown in Fig. 3e bottom, similar Co L_3/L_2 ratios (~4.68) are determined for R1-4. Then, the ratio increases and reaches ~5.4 at R6. However, all the determined ratios suggest a pure Co^{2+} inside the GCFCO.

Tilting a CGO20 grain along [101] direction, the CGO20-GCFCO interface in Fig. 4a enables a close look of the CGO20 part. Similar as in Fig. 3a, the interface is clean, and the CGO20 edge can be well outlined using its (010) and (11-1) planes. By EELS SI, the atomic columns on the CGO20 side are clearly resolved in Fig. 4b. Again, ~1 nm thick Co and Gd are segregated to the edges as shown in
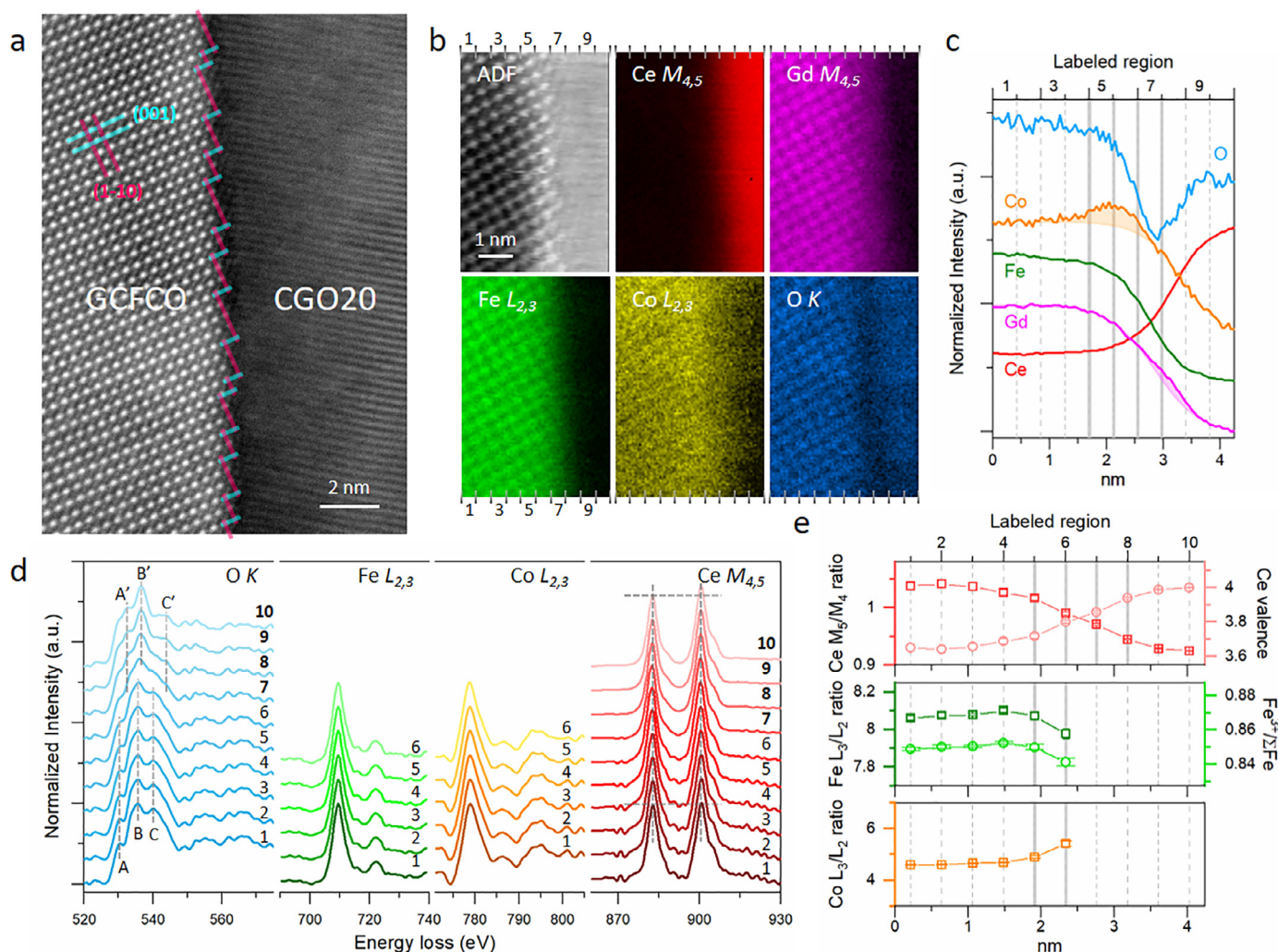
Fig. 3. The CGO20-GCFCO interface inside 60CGO20-FC2O. (a) HAADF image showing the atomic structure of the interface: the left GCFCO along its [110] zone axis and the right CGO20 randomly oriented. Edge of the GCFCO is outlined by its (001) and (1-10) planes, as indicated by the two pairs of lines. (b) The EELS SI results from the interface: the simultaneously recorded ADF image, and the extracted elemental maps in intensity from Ce $M_{4,5}$, Gd $M_{4,5}$, Fe $L_{2,3}$, Co $L_{2,3}$ and O K edges. The whole mapping area is divided into ten sub-regions, R1-10, as labeled at the top of the ADF image. (c) Vertically averaged intensity profiles of Ce, Gd, Fe, Co and O based on the elemental maps in (b). The filled areas below the Co and Gd profiles suggest segregations at the edge of GCFCO and CGO20 respectively. (d) The integrated EEL spectra from each sub-region. (e) The estimated valence states for Ce, Fe and Co. Error bars were calculated using the standard errors of integrated Ce $M_{4,5}$, Fe $L_{2,3}$ and Co $L_{2,3}$ intensity values.

Fig. 4c, indicating an interface between R3 and R4. For the O K edges in Fig. 4d, similar peaks A-C from R1-3 (GCFCO side) and A'-C' from R4-8 (CGO20 side) as in Fig. 3d can be recognized. Only Fe $L_{2,3}$ and Co $L_{2,3}$ edge from R1 are plotted in Fig. 4e, due to the already noisy signals close to the interface. Difference among the Ce $M_{4,5}$ edges from each sub-region is rather small in Fig. 4d, which is also reflected in Fig. 4f. The Ce valence increases from ∼3.66 at R1 and reaches already ∼4 at R5. Thus, on the CGO20 side, pure Ce^{4+} is well kept even <1 nm away from the edge. A minimum drop to ∼3.92 is noticed at R4.

3.4. The composition of CGO and the CGO grain boundaris

Formation of the GCFCO requires sufficient Gd, which can only come from the primary CGO phase. Thus, the effective compositions of the CGOs are checked. Taking the nominal composition $Ce_{0.9}Gd_{0.1}O_{2-\delta 1}$ of the CGO10 inside 85CGO10-FC2O as a reference, the CGO20 inside 85CGO20-FC2O is determined as $Ce_{0.88}Gd_{0.12}O_{2-\delta 2}$, while the 2-$\delta$1 value is higher than the 2-δ2 by a factor of 1.14 (Supporting information, Fig. S5 and Table S1).

A typical CGO20 GB within 85CGO20-FC2O is shown in Fig. 5a. The bottom grain, G2, is oriented along the [101] direction and

thus appears brighter than the top CGO20 grain, G1, which is randomly oriented. Based on the EDX chemical mapping, a significant loss of Ce as well as evident enrichments of Gd, Fe and Co are detected simultaneously at the GB. Along the arrow in Fig. 5a, laterally averaged intensity profile of each element is further plotted in Fig. 5b. In addition to the features already obvious in Fig. 5a, considerable Gd is segregated to the edges of both grains, as suggested by the two peaks along the Gd profile. Bulges around the GB are noticed for both Fe and Co, but with much lower intensities comparing with Ce and Gd. All these chemical disorders are mainly confined within the shadowed region in Fig. 5b, ∼3.5 nm wide.

Similar features are also observed for many CGO10 GBs in 85CGO10-FC2O (Supporting information, Fig. S5). In addition, significant segregations of Fe and Co are often noticed, and one example is shown in Fig. 5c. Both the CGO10 grains, G3 and G4, are randomly oriented. Along the GB, discontinuous features with dark contrast are obvious in the HAADF image, which are mainly rich in Fe and Co as revealed by the EDX chemical mapping. Elemental profiles across the interface are vertically averaged and plotted in Fig. 5d. The Ce shows a broad drop at the GB, while any change along the Gd or O profile is rather ignorable. In contrast to Fig. 5b,
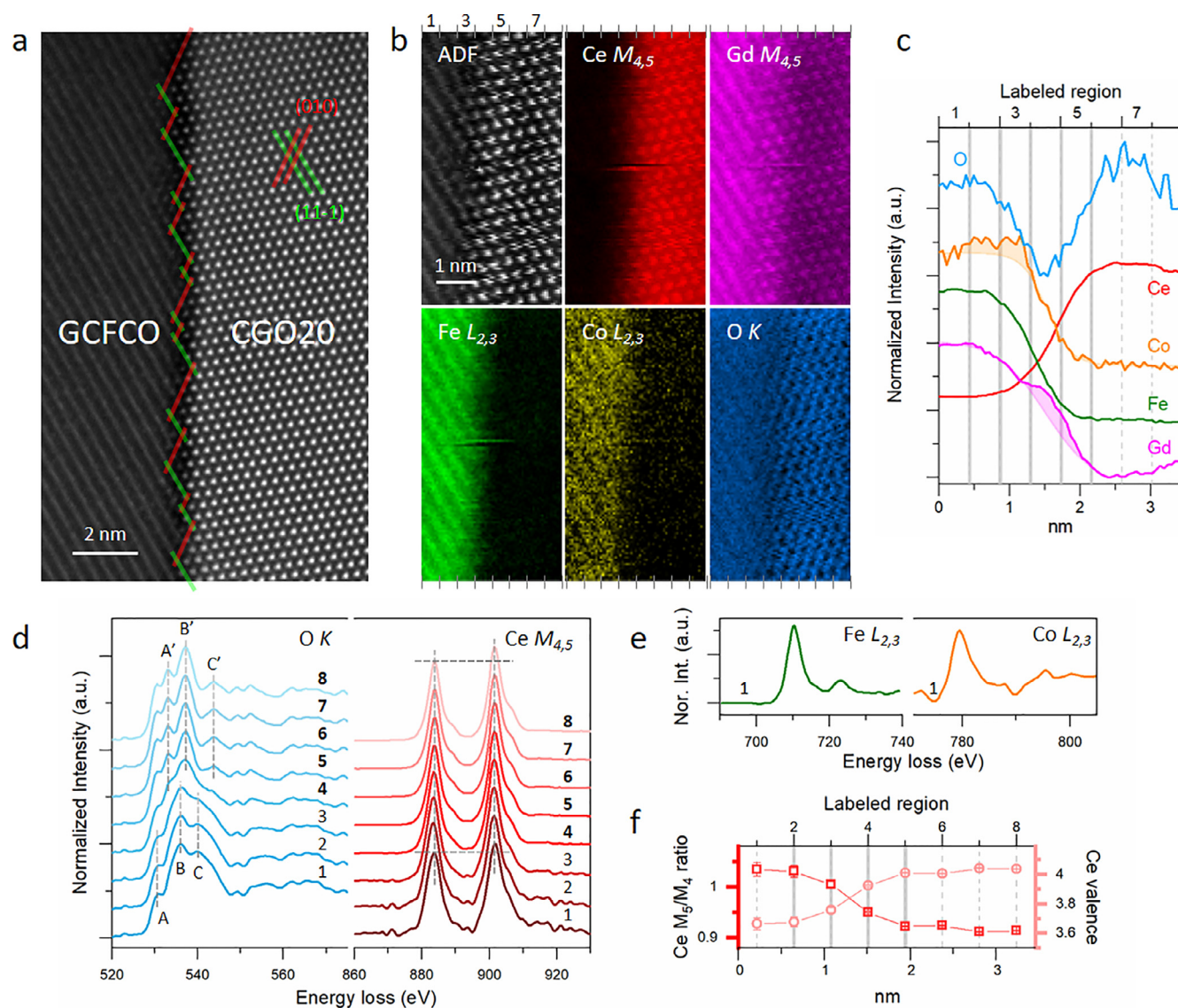
Fig. 4. The CGO20-GCFCO interface inside 85GO20-FC2O. (a) HAADF image showing the atomic structure of the interface: the right CGO20 along its [101] direction and the left GCFCO randomly oriented. Edge of the CGO20 is outlined by its (010) and (11-1) planes, as indicated by the two pairs of lines. (b) The EELS SI results from the interface: the simultaneously recorded ADF image, and the extracted elemental maps in intensity from Ce $M_{4,5}$, Gd $M_{4,5}$, Fe $L_{2,3}$, Co $L_{2,3}$ and O K edges. The whole mapping area is divided into eight sub-regions, R1-8, as labeled at the top of the ADF image. (c) Vertically averaged intensity profiles of Ce, Gd, Fe, Co and O based on the elemental maps in (b). The filled areas below the Co and Gd profiles suggest segregation at the edge of GCFCO and CGO20 respectively. (d) The integrated O K and Ce $M_{4,5}$ edges from each sub-region. (e) The integrated Fe $L_{2,3}$ and Co $L_{2,3}$ edge from R1. (f) The estimated valence states for Ce. Error bars were calculated using the standard errors of integrated Ce $M_{4,5}$ intensity values.

both Fe and Co enrich significantly around the GB in Fig. 5d. Their peaks are exceeding the Gd curve, and ~18 nm wide as highlighted by the shadow.

4. Discussion

The emerging phase inside DP-OTM is considered as a product of the interaction between the two primary phases [9,38–40]. As already shown in Fig. 1, GCFCO is formed inside the 85CGO20-FC2O, and predominately surrounded by the CGO20 grains, while no additional phase is observed within 85CGO10-FC2O. The GCFCO consumes a significant portion of Gd from the initial CGO20, resulting in a CGO phase determined as $Ce_{0.88}Gd_{0.12}O_{2-\delta}$ as compared with the $Ce_{0.9}Gd_{0.1}O_{2-\delta}$ in 85CGO10-FC2O. During the initial densification of CGO, both Fe and Co migrate to the CGO GBs. As the sintering proceeds, most of them segregate out from CGO GBs and form the Co-rich spinel phase, while the residual Co and Fe stay at

the CGO GBs as non-solute segregations. Along the CGO20 GBs, the segregated Fe and Co are only around several nms thick, while significant Fe and Co are often noticed at the CGO10 GBs as in Fig. 5c and d. Such behaviors were also observed for CGO20-FC2Os with higher CGO20 content [19]. The similar Gd contents in both CGO10 and CGO20 suggest that the formation of GCFCO relies on an initial Gd content in CGO above ~10 mol%. Thus, using CGO20 as raw material, the 85CGO20-FC2O possesses considerable excessive Gd, which is usually enriched at the CGO edges together with migrated Fe and Co as shown in Fig. 5a. With all the necessary and sufficient chemistries, GCFCO then forms directly next to CGO20. In contrast, for 85CGO10-FC2O, the initial Gd would be insufficient, which hinders the formation of GCFCO and leaving often significant Fe and Co segregation as in Fig. 5c and d. Aparently, Gd doping could be controlled to manipulate the GCFCO formation, which affects the segeration of Fe and Co as well as Gd at the CGO GBs, and finally the ionic and/or electronic conductivity.
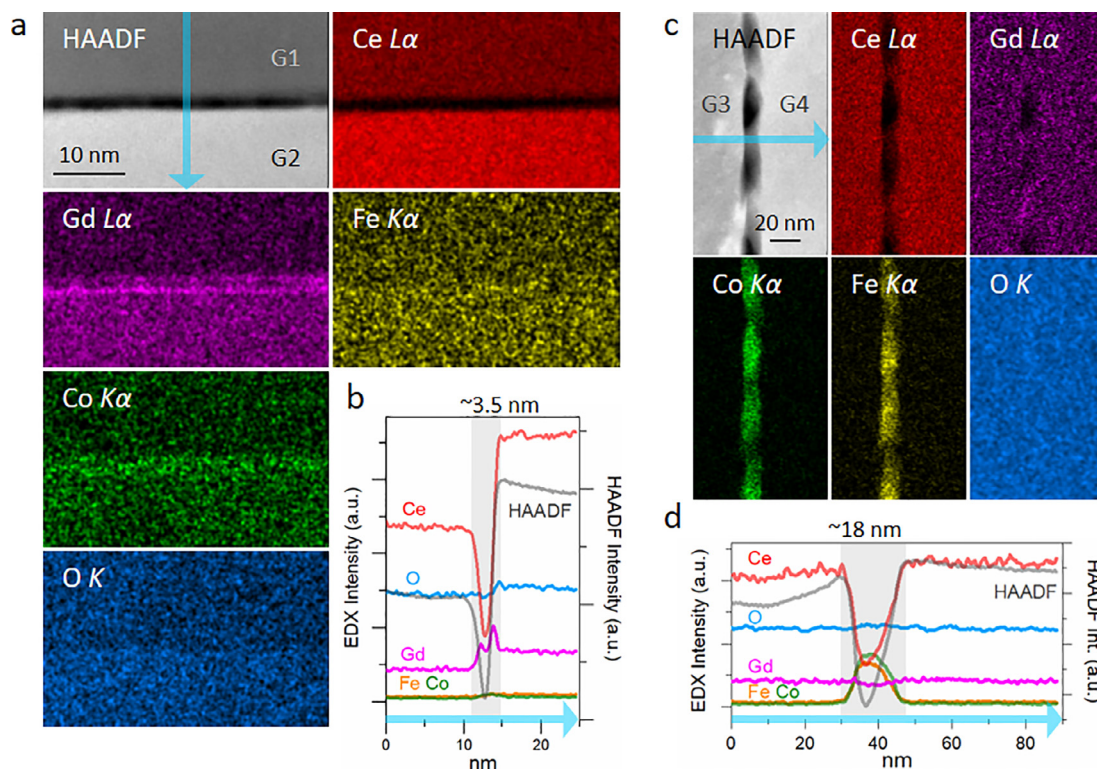
Fig. 5. The CGO GBs. (a) The EDX chemical mapping results from a typical CGO20 GB: HAADF image and the elemental maps in intensity from the Ce $L\alpha$ line, Gd $L\alpha$ line, Fe $K\alpha$ line, Co $K\alpha$ line and O K line. The top grain, G1, is randomly oriented, while the lower grain, G2, is along the [101] direction. (b) Laterally averaged intensity profiles across the CGO20 GB, as indicated by the arrow in (a). (c) The EDX chemical mapping results around a CGO10 GB. Both grains are randomly oriented. (d) Vertically averaged intensity profiles across the CGO10 GB, as indicated by the arrow in (c).

Depending on the nominal ratio of CGO20 and FC2O (r), both x and y of the emerging phase $Gd_{1-x}Ce_xFe_{1-y}Co_yO_{3-\delta}$ vary [24]. As shown in Table 1, the Fe and Ce valence as well as oxygen vacancies of the emerging phase are all sensitive to x and y, and thus to r. Moreover, the GCFCO grain in 60CGO20-FC2O (see Fig. 3) are determined as $Gd_{0.65}Ce_{0.35}Fe_{0.72}Co_{0.28}O_{3-\delta}$ (Supporting information, Fig. S6 and Table S2). As in Fig. 3e, different Ce valence of ~3.65 and the $Fe^{3+}/\Sigma Fe$ ratio of ~85% are determined as compared with Table 1. Therefore, a fine tuning of the GCFCO could be realized through carefully adapting the CGO and FC2O including their chemical compositions as well as the weight ratio. The tunable electronic properties of GCFCO revealed here would also support its promising employment as a primary phase for many other DP-OTMs.

Disordered features along the interface are unfavorable for any OTMs, as both oxygen ionic and electronic conductivities can be strongly affected. Around the CGO20-GCFCO interfaces in Figs. 3 and 4, structural defect is rather ignorable, while only slight Co and Gd ~1 nm segregated to the edges. On the GCFCO side, constant valence states of Fe, Co and Ce were observed. Only close to the interface where Co enriches, the Ce valence starts to increase. On the CGO20 side, coinciding with the Gd enrichment, the slightly decreased Ce valence recovers quickly to 4, and up to $Ce^{3.92+}$ is determined directly at the CGO20 edge. For comparison, $Ce^{3.40+}$ is determined at a CGO20 GB, where intact crystal structure and similar chemical distributions as in Figs. 3 and 4 are observed (Supporting information, Fig. S7). Thus, the CGO20 is comparably or even less affected by the adjacent GCFCO than by its own type. With the conducting behaviors of GCFCO successfully tuned, the emerging phase could serve as a promising promoter for the oxygen transport.

5. Conclusions

In summary, emerging phase GCFCO was identified for 85CGO20-FC2O, instead of 85CGO10-FC2O. Formation of the GCFCO significantly reduces Fe and Co segregation at the CGO20 GBs, and introduces extra CGO20-GCFCO interfaces. Any structural defects at these newly introduced interfaces are ignorable while chemical disorders including elemental segregations and valence state variations are mainly limited within ~1 nm. Together with its tunable electronic properties, the GCFCO broadens the opportunity for membrane optimization through phase engineering. Our findings compose a crucial piece for the complete picture of phase interaction and interface properties inside the CGO-FC2O composites, which could also be good examples for a series of multiphase composites.

Declaration of Competing Interest

The authors declare that they have no known competing financial interests or personal relationships that could have appeared to influence the work reported in this paper.

Supplementary materials

Supplementary material associated with this article can be found, in the online version, at doi:10.1016/j.actamat.2022.118034.

References

[1] G.X. Chen, A. Feldhoff, A. Weidenkaff, C. Li, S.M. Liu, X.F. Zhu, J. Sunarso, K. Huang, X.Y. Wu, A.F. Ghoniem, W.S. Yang, J. Xue, H.H. Wang, Z.P. Shao, J.H. Duffy, K.S. Brinkman, X.Y. Tan, Y. Zhang, H.Q. Jiang, R. Costa, K.A. Friedrich, R. Kriegel, Roadmap on sustainable mixed ionic-electronic conducting membranes, Adv. Funct. Mater. 32 (2021) 2105702.

[2] X.F. Zhu, W.S. Yang, Microstructural and ínterfacial designs of oxygen-permeable membranes for oxygen separation and reaction-separation coupling, Adv. Mater. 31 (50) (2019) 1902547.

[3] F. Buck, A. Feldhoff, J. Caro, T. Schiestel, Permeation improvement of LCCF hollow fiber membranes by spinning and sintering optimization, Sep. Purif. Technol. 259 (2021) 118023.

[4] J. Xue, G.W. Weng, L. Chen, Y.P. Suo, Y.Y. Wei, A. Feldhoff, H.H. Wang, Various influence of surface modification on permeability and phase stability through an oxygen permeable membrane, J. Membr. Sci. 573 (2019) 588.

[5] M. Ramasamy, E.S. Persoon, S. Baumann, M. Schroeder, F. Schulze-Kuppers, D. Gortz, R. Bhave, M. Bram, W.A. Meulenberg, Structural and chemical stability of high performance $Ce_{0.8}Gd_{0.2}O_{2-\delta}$ - $FeCo_2O_4$ dual phase oxygen transport membranes, J. Membr. Sci. 544 (2017) 278.

[6] M. Balaguer, J. Garcia-Fayos, C. Solis, J.M. Serra, Fast oxygen separation through SO_2- and CO_2-stable dual-phase membrane based on $NiFe_2O_4$-$Ce_{0.8}Tb_{0.2}O_{2-\delta}$, Chem. Mater. 25 (2013) 4986.

[7] H.X. Luo, K. Efimov, H.Q. Jiang, A. Feldhoff, H.H. Wang, J. Caro, CO_2-stable and cobalt-free dual-phase membrane for oxygen separation, Angew. Chem. Int. Ed. 50 (2011) 759.

[8] F.L. Zeng, J. Malzbender, S. Baumann, W.Y. Zhou, M. Ziegner, A. Nijmeijer, O. Guillon, R. Schwaiger, W.A. Meulenberg, Mechanical reliability of $Ce_{0.8}Gd_{0.2}O_{2-\delta}$-$FeCo_2O_4$ dual phase membranes synthesized by one-step solid-state reaction, J. Am. Ceram. Soc. 104 (4) (2021) 1814.

[9] Y. Lin, S.M. Fang, D. Su, K.S. Brinkman, F.L. Chen, Enhancing grain boundary ionic conductivity in mixed ionic-electronic conductors, Nat. Commun. 6 (2015) 6824.

[10] F.L. Zeng, S. Baumann, J. Malzbender, A. Nijmeijer, L. Winnubst, O. Guillon, R. Schwaiger, W.A. Meulenberg, Enhancing oxygen permeation of solid-state reactive sintered $Ce_{0.8}Gd_{0.2}O_{2-\delta}$-$FeCo_2O_4$ composite by optimizing the powder preparation method, J. Membr. Sci. 628 (2021) 119248.

[11] F.L. Zeng, J. Malzbender, S. Baumann, A. Nijmeijer, L. Winnubst, M. Ziegner, O. Guillon, R. Schwaiger, W.A. Meulenberg, Optimization of sintering conditions for improved microstructural and mechanical properties of dense $Ce_{0.8}Gd_{0.2}O_{2-\delta}$-$FeCo_2O_4$ oxygen transport membranes, J. Eur. Ceram. Soc. 41 (1) (2021) 509.

[12] H.X. Luo, H.Q. Jiang, T. Klande, Z.W. Cao, F.Y. Liang, H.H. Wang, J. Caro, Novel cobalt-free, noble metal-free oxygen-permeable $40Pr_{0.6}Sr_{0.4}FeO_{3-\delta}$-$60Ce_{0.9}Pr_{0.1}O_{2-\delta}$ dual-phase membrane, Chem. Mater. 24 (2012) 2148.

[13] X.F. Zhu, H.H. Wang, W.S. Yang, Relationship between homogeneity and oxygen permeability of composite membranes, J. Membr. Sci. 309 (2008) 120.

[14] W. Fang, F.Y. Liang, Z.W. Cao, F. Steinbach, A. Feldhoff, A mixed ionic and electronic conducting dual-phase membrane with high oxygen permeability, Angew. Chem. Int. Ed. 54 (16) (2015) 4847.

[15] D.R. Ou, T. Mori, F. Ye, T. Kobayashi, J. Zou, G. Auchterlonie, J. Drennan, Oxygen vacancy ordering in heavily rare-earth-doped ceria, Appl. Phys. Lett. 89 (17) (2006) 171911.

[16] H.C. Du, C.L. Jia, J. Mayer, J. Barthel, C. Lenser, R. Dittmann, Atomic structure of antiphase nanodomains in Fe-doped $SrTiO_3$ films, Adv. Funct. Mater. 25 (40) (2015) 6369.

[17] K. Ran, W. Deibert, M.E. Ivanova, W.A. Meulenberg, J. Mayer, Direct observation of the grain boundary segregation in molybdenum substituted lanthanum tungstate membranes, Nanoscale 12 (2020) 17841.

[18] K. Ran, W. Deibert, H.C. Du, D. Park, M.E. Ivanova, W.A. Meulenberg, J. Mayer, Processing-induced secondary phase formation in Mo-substituted lanthanum tungstate membranes, Acta Mater. 180 (2019) 35.

[19] K. Ran, L. Fischer, S. Baumann, W.A. Meulenberg, K. Neuhaus, J. Mayer, Tuning the ceria interfaces inside the dual phase oxygen transport membranes, Acta Mater. 226 (2022) 117603.

[20] B. Feng, T. Yokoi, A. Kumamoto, M. Yoshiya, Y. Ikuhara, N. Shibata, Atomically ordered solute segregation behaviour in an oxide grain boundary, Nat. Commun. 7 (2016) 11079.

[21] P. Gao, S.Z. Yang, R. Ishikawa, N. Li, B. Feng, A. Kumamoto, N. Shibata, P. Yu, Y. Ikuhara, Atomic-scale measurement of flexoelectric polarization at $SrTiO_3$ dislocations, Phys. Rev. Lett. 120 (26) (2018) 267601.

[22] H.C. Du, C.L. Jia, L. Houben, V. Metlenko, R.A. De Souza, R. Waser, J. Mayer, Atomic structure and chemistry of dislocation cores at low-angle tilt grain boundary in $SrTiO_3$ bicrystals, Acta Mater. 89 (2015) 344.

[23] F.L. Zeng, J. Malzbender, S. Baumann, A. Nijmeijer, L. Winnubst, O. Guillon, R. Schwaiger, W.A. Meulenberg, Residual stress and mechanical strength of $Ce_{0.8}Gd_{0.2}O_{2-\delta}$-$FeCo_2O_4$ dual phase oxygen transport membranes, J. Eur. Ceram. Soc. 41 (13) (2021) 6539.

[24] L. Fischer, K. Neuhaus, C. Schmidt, K. Ran, P. Behr, S. Baumann, J. Mayer, W.A. Meulenberg, Phase formation and performance of solid state reactive sintered $Ce_{0.8}Gd_{0.2}O_{2-\delta}$-$FeCo_2O_4$ composites, J. Mater. Chem. A 10 (2022) 2412.

[25] A. Buchheit, B. Tessmer, K. Ran, J. Mayer, H.D. Wiemofer, K. Neuhaus, The impact of Fe addition on the electronic conductivity of gadolinium doped ceria, ECS J. Solid State Sci. Technol. 8 (1) (2019) 41.

[26] A. Kovács, R. Schierholz, K. Tillmann, FEI Titan G2 80-200 CREWLEY, J. Large Scale Res. Facil. 2 (2016) A43.

[27] K. Momma, F. Izumi, VESTA 3 for three-dimensional visualization of crystal, volumetric and morphology data, J. Appl. Crystallogr. 44 (2011) 1272.

[28] N.L. Ross, J. Zhao, R.J. Angel, High-pressure structural behavior of $GdAlO_3$ and $GdFeO_3$ perovskites, J. Solid State Chem. 177 (10) (2004) 3768.

[29] J.A. Fortner, E.C. Buck, The chemistry of the light rare-earth elements as determined by electron energy loss spectroscopy, Appl. Phys. Lett. 68 (1996) 3817.

[30] P.F. Yan, T. Mori, Y.Y. Wu, Z.M. Li, G.J. Auchterlonie, J. Zou, J. Drennan, Microstructural and chemical characterization of ordered structure in yttrium doped ceria, Microsc. Microanal. 19 (2013) 102.

[31] P.A. van Aken, B. Liebscher, Quantification of ferrous/eerric ratios in minerals: new evaluation schemes of Fe L_{23} electron energy-loss near-edge spectra, Phys. Chem. Miner. 29 (2002) 188.

[32] D.H. Pearson, C.C. Ahn, B. Fultz, White lines and D-electron occupancies for the 3d and 4d transition-metals, Phys. Rev. B 47 (14) (1993) 8471.

[33] Z.L. Wang, J.S. Yin, Y.D. Jiang, EELS analysis of cation valence states and oxygen vacancies in magnetic oxides, Micron 31 (5) (2000) 571.

[34] X. Guo, R. Waser, Electrical properties of the grain boundaries of oxygen ion conductors: acceptor-doped zirconia and ceria, Prog. Mater. Sci. 51 (2006) 151.

[35] H.J. Avila-Paredes, K. Choi, C.T. Chen, S. Kim, Dopant-concentration dependence of grain-boundary conductivity in ceria: a space-charge analysis, J. Mater. Chem. 19 (2009) 4837.

[36] M. Chen, B. Hallstedt, A.N. Grundy, L.J. Gauckler, CeO_2-CoO phase diagram, J. Am. Ceram. Soc. 86 (9) (2003) 1567.

[37] T.S. Zhang, P. Hing, H.T. Huang, J. Kilner, Densification, microstructure and grain growth in the CeO_2-Fe_2O_3 system ($0 <= Fe/Ce <= 20\%$), J. Eur. Ceram. Soc. 21 (12) (2001) 2221.

[38] M. Ramasamy, S. Baumann, A. Opitz, R. Iskandar, J. Mayer, D. Udomsilp, U. Breuer, M. Bram, Phase interaction and distribution in mixed ionic and electronic conducting ceria-spinel composites, in: Advances in Solid Oxide Fuel Cells and Electronic Ceramics II, 37, 2017, p. 99.

[39] M. Ramasamy, S. Baumann, J. Palisaitis, F. Schulze-Kuppers, M. Balaguer, D. Kim, W.A. Meulenberg, J. Mayer, R. Bhave, O. Guillon, M. Bram, Influence of microstructure and surface activation of dual-phase membrane $Ce_{0.8}Gd_{0.2}O_{2-\delta}$-$FeCo_2O_4$ on oxygen permeation, J. Am. Ceram. Soc. 99 (1) (2016) 349.

[40] F.L. Zeng, J. Malzbender, S. Baumann, M. Kruger, L. Winnubst, O. Guillon, W.A. Meulenberg, Phase and microstructural characterizations for $Ce_{0.8}Gd_{0.2}O_{2-\delta}$-$FeCo_2O_4$ dual phase oxygen transport membranes, J. Eur. Ceram. Soc. 40 (15) (2020) 5646.